Potential Vorticity of Flow along the Alps

ALAN J. THORPE

Joint Centre for Mesoscale Meteorology, Department of Meteorology, University of Reading, England

HANS VOLKERT AND DIETRICH HEIMANN

Institut für Physik der Atmosphäre, DLR, Oberpfaffenhofen, Germany

(Manuscript received 28 April 1992, in final form 18 August 1992)

ABSTRACT

Observations from the German Front Experiment are presented here that show the existence—in conditions with a dominant flow component parallel to the main Alpine chain—of a mesoscale region to the north of the Alps where the absolute and potential vorticity (PV) are substantially negative. These structures exist before the front arrives to the Alps and appear to be affected little by the passage of the front. A dynamical explanation for these and other mesoscale structures is sought by considering a simple unsheared airflow impinging on the Alps from the west. A linear frictionless model for the steady-state response is used as well as a full nonlinear numerical model with and without friction. A vastly simplified Alpine orography is considered as well as one that adequately describes its mesoscale detail.

The results show that the frictionless linear dynamics lead to a zone north of the Alps with anticyclonic vorticity but with uniform (positive) potential vorticity. With boundary-layer processes included in a nonlinear simulation substantial PV anomalies are produced. This leads to negative PV, and absolute vorticity, north of the Alps and positive PV south of the Alps. The region of PV anomalies in the model bears a suggestive similarity to that in the observations. The PV structures are attributed to frictional processes acting in a boundary layer that acquires a slope due to the sloping mountain sides. This mechanism only operates in this situation.

Other mesoscale aspects of the flow are discussed in regions around the Alps for which we have as yet no detailed observational evidence; for example, there is strong flow retardation immediately downstream of the orography. An important conclusion is that the Alps, in conditions of parallel flow, are a significant source of potential vorticity anomalies in the lower troposphere. These are advected away from the orography and must be an important part of the tropospheric PV budget.

1. Introduction

In this paper aspects of the mesoscale dynamics of flow impinging almost parallel to the Alps will be considered. The stimulii for this study are the observations made during the German Front Experiment in 1987; see Hoinka and Volkert (1987 and 1992) for further details of this campaign. A primary objective of that project was to better understand the modification to fronts and their passage as they become influenced by the Alps; see Egger and Hoinka (1992). In this paper, however, we focus on mesoscale structures north of the Alps present before and during frontal passage. We will not consider the dynamics of the front per se. First, a mesoscale objective analysis of the radiosonde data obtained in the German Front Experiment is presented for three cases. These data were obtained from a mesoscale network of soundings in the north Alpine region. These events took place on 8 October (IOP-A), 12 November (IOP-B), and 18/19 December 1987 (IOP-D). The objective analysis allows derived fields such as vorticity and potential vorticity to be deduced. Here only those aspects of these analyses relevant to the problem to be considered will be described.

We concentrate on the flow ahead of the front, which is commonly from the southwesterly sector and oriented approximately *along the axis* of the Alpine chain. The main ridge of the Alps is oriented along 260° → 80°. In Table 1 wind speed and direction are given at several levels from soundings made in the three IOPs at Payerne, west of the Alps, and Munich, north of the Alps. These data show the dominance of the alongridge wind component in the prefrontal air. The objective analysis to be presented in the next section shows that there is notably strong anticyclonic vorticity ahead of the front in the lower and midtroposphere, in the observational region north of the Alps, which is only temporarily modified by the frontal passage. In fact, the absolute vorticity is often negative, as is the potential vorticity. These features are not typical of prefrontal flow in fronts approaching the continent from the ocean; see Thorpe and Clough (1991). In that paper,

Corresponding author address: Prof. Alan J. Thorpe, Department of Meteorology, University of Reading, 2 Earley Gate, Whiteknights, P.O. Box 239, Reading, RG6 2AU, England.

TABLE 1. Speed (ff), direction (dd), alongridge u and cross-ridge v components of prefrontal wind velocity in three levels above Payerne (PA), and München–Oberschleißheim (MO) for IOPs A, B, and D. The main Alpine ridge is oriented 260°→ 80°.

	PA				MO			
Level (hPa)	ff (m s^{-1})	dd (deg)	u (m s^{-1})	v (m s^{-1})	ff (m s^{-1})	dd (deg)	u (m s^{-1})	v (m s^{-1})
				IOP A, 0600 UTC				
500	29.5	230	25.5	14.7	16.5	230	14.3	8.2
700	31.0	235	28.1	13.1	16.5	240	15.5	5.6
850	23.0	215	16.3	16.3	5.2	190	1.8	4.9
				IOP B, 1200 UTC				
500	39.0	260	39.0	0.0	33.0	245	31.9	2.9
700	34.0	255	33.9	3.0	7.5	255	7.4	1.5
850	24.5	225	21.2	12.2	7.2	230	6.3	3.6
				IOP D, 0000 UTC				
500	24.5	250	24.1	4.3	21.6	275	20.9	−5.6
700	26.5	255	26.4	2.3	23.2	270	22.8	−4.0
850	18.0	260	18.0	0.0	19.6	270	19.2	−3.4

observations are presented from the Fronts 87 experiment showing the existence of a strong *positive* PV anomaly at low levels immediately ahead of cold fronts. It becomes clear, therefore, that any understanding of Alpine influences on fronts needs to begin with an understanding of the factors that determine the prefrontal Alpine flow. This brings us to the main topic to be considered in this paper—namely, to use linear and nonlinear models to describe and understand the dynamics of prefrontal airflow, which is primarily along the Alpine chain. Diagnoses from the European Centre for Medium-Range Weather Forecasts T-213 model are also presented, which show the existence in a forecast model of the regions of negative potential vorticity.

It is apparent from the literature that the problem of airflow approximately parallel to a mesoscale mountain range, such as the Alps, has not been considered. There has been much work considering flow over ridges oriented perpendicular to the flow and of flow over small-scale isolated orography with approximately circular contours. Smith (1982) discusses the problem of mesoscale mountain flows, including those over the Alps, but does not examine the parallel flow case. Another aspect of published work is that almost all linear and nonlinear studies consider inviscid flow. While this obviates the necessity to consider the boundary-layer structure, which over complex terrain is an extremely difficult problem, it means that the published results may have little to do with reality. In this paper we intend to begin to fill some of these gaps in our knowledge.

Relatively little attention has been given to the vertical vorticity and potential vorticity structure of the flow around mesoscale mountains where the earth's rotation has a significant role. The Ertel potential vorticity, $\mathrm{PV} = \rho^{-1}\boldsymbol{\zeta}\cdot\nabla\theta$, is conserved in adiabatic frictionless flow. In this paper we will consider diagnoses of the vertical component of absolute vorticity, ζ, and the potential vorticity. The relationship between these can be seen by rewriting the expression for the PV in the following way:

$$\mathrm{PV} = \frac{1}{\rho}\left(\zeta\frac{\partial\theta}{\partial z} + \boldsymbol{\zeta}_h\cdot\nabla_h\theta\right), \tag{1}$$

where $\boldsymbol{\zeta}_h$ is the horizontal component of the vorticity. The analyses presented in the next section reveal regions where both ζ and PV are negative. For a region with negative ζ, given that the static stability is positive in these cases, the sign of the PV depends on the relative contribution of the $\boldsymbol{\zeta}_h$ terms. The nature of these terms can be seen more clearly if the vertical-velocity contributions to $\boldsymbol{\zeta}_h$ are ignored as they are small. Then the horizontal vorticity is made up of the components of the vertical wind shear. Using the thermal wind equations to express the thermal gradient in terms of the geostrophic wind shear we obtain the following expression for the PV:

$$\mathrm{PV} \approx \frac{1}{\rho}\left\{\zeta\frac{\partial\theta}{\partial z} - \frac{f\theta_0}{g}\left[\left(\frac{\partial u_g}{\partial z}\right)^2 + \left(\frac{\partial v_g}{\partial z}\right)^2 + \frac{\partial u_{ag}}{\partial z}\frac{\partial u_g}{\partial z} + \frac{\partial v_{ag}}{\partial z}\frac{\partial v_g}{\partial z}\right]\right\}, \tag{2}$$

where suffices g and ag refer to the geostrophic and ageostrophic components of the flow, respectively. If the flow is geostrophic then the $\boldsymbol{\zeta}_h$ terms would reduce the PV further. However, for mountain flows the ageostrophic wind shear terms can be large. The horizontal vorticity contribution to the PV is then also determined

by the correlation between the ageostrophic and geostrophic shear.

With friction and diabatic processes the potential vorticity is, of course, no longer conserved. The evolution of PV is given by the following equation:

$$\frac{D\mathrm{PV}}{Dt} = \frac{1}{\rho}(\nabla\theta \cdot \nabla \times \mathbf{F} + \zeta \cdot \nabla\dot{\theta}), \qquad (3)$$

where $\mathbf{F}$ is the frictional force and $\dot{\theta}$ is the diabatic source term. In a frictional boundary layer the diabatic and frictional terms are nonzero, and upstream of a mountain range the boundary layer is in an approximate turbulent equilibrium. This implies a reduction in the PV of the boundary layer over about the lowest kilometer; the boundary layer has low static stability and low potential vorticity approaching the mountain. The implications of frictional processes for the potential vorticity structure at fronts have been discussed recently by Cooper et al. (1992). They show that it is commonly the case that the frictional effects in strong baroclinic zones act to generate a local *maximum* in PV. This again indicates that the zones of negative PV that we find in the analyses of observations in the Alpine foreland, to be presented here, are not likely to be associated with the incoming fronts. Rather, they are a direct result of the mountain perturbation of the flow.

Thorsteinsson (1988) has described the nonlinear structure of flow past a symmetrical isolated mesoscale mountain. These numerical model results are for an isentropic mountain for a frictionless flow with uniform potential vorticity. For certain values of Rossby and Froude number the flow exhibits a "collapsed" region in which the static stability is extremely large and the absolute vorticity is close to zero. This zone extends from the mountain summit to its lee. While of interest, these results are of limited use for the Alpine flow discussed here due to the assumptions of an isentropic lower boundary condition and of uniform potential vorticity.

There has recently been interest in the literature concerning the generation of lee vortices and wakes and the role of hydraulic jumps and wave breaking in that process; see Smolarkiewicz and Rotunno (1989), Smith (1989), Schär and Smith (1993a,b), and Schär (1993). This concerns low Froude number flow, and the generation of potential vorticity, by dissipative processes, in the wake region has been discussed. This research is potentially of interest in providing a possible explanation for the PV anomalies in the Alpine observations presented here. The conclusion is reached that these effects are probably not as effective as those associated with the frictional boundary layer and appear not to be operating for the flow regime discussed here.

2. Objective analysis of mesoscale observations

Observations from any radiosonde network are irregularly spaced in the horizontal and vertical directions, because the stations are not regularly distributed and the reported significant points are situated at different levels. It is, therefore, necessary to interpolate the observations of the primary variables onto a regular three-dimensional grid, if sections of derived quantities are sought. In this section the mathematical method is outlined, sample results from IOPs A, B, and D are presented, and conclusions are drawn pointing to more general questions concerning airflow along a mountain range.

a. Mathematical method

A variety of techniques is available for objective spatial data analysis. Thiebaux and Pedder (1987) give a detailed overview. Very common are statistical or optimum interpolation methods, especially for hemispheric and global-scale weather forecasting. An analyzed gridpoint value consists of a prescribed first-guess field evaluated at the grid point plus an interpolated analysis error, which contains weighted differences between observations and first guess within a certain area around the grid point. Lanzinger and Steinacker (1990) have applied such a technique for the mesoα-scale analysis of radiosonde data from the ALPEX period. In the vicinity of the Alps, they constructed anisotropic weighting functions, which take into account the position of the mountain block relative to the grid point under consideration.

We, on the contrary, follow a function surface-fitting approach using three-dimensional surfaces. First, from the positions (in three-dimensional space) of the complete set of reported significant points, weighting factors are set up from all synchronous soundings. Then the values of spline surface parameters are calculated taking into account the weighting factors, the observations of the meteorological variable in question, and a prescribed root-mean-square difference between all observations and their respective estimates. Finally, the spline surface parameters are used to gain values for the meteorological fields at regularly distributed grid points in the three-dimensional space covered by the observations. The mathematical properties of this three-stage process are given in Thiebaux and Pedder (1987, pp. 62–71) and, in more detail, in the appendices of Wahba and Wendelberger (1980). To be specific, we used spline surfaces of order 2 and prescribed 0.5 K, 1.0 K, 1 m s^{-1} as root-mean-square differences for temperature, dewpoint, and the velocity components, respectively.

It is important to note that the spline surface method, as applied here, relies only on information contained in a single realization of a spatial distribution, whereas statistical interpolation methods require a prescribed model for spatial covariance and a first-guess field. Thus, the latter are appropriate for operational environments, where a first guess is, for example, taken from the latest forecast model run, while the spline

surface approach appears to be better suited for observational case studies.

b. *Results for IOPs A, B, and D*

The analyses of the radiosonde data from three cases of the German Front Experiment will now be presented. The area of the analysis and location of the soundings is given in Fig. 1; note that not all stations reported at all times and then only to varying ceiling heights. Typically the soundings were made every 3 hours.

Equivalent potential temperature θ_e at the 850-hPa level is used to mark the general progression of the cold fronts north of the Alpine baseline and below crest height. During IOP-A the front entered the area of dense observations from the west between 0600 and 0900 UTC; see Fig. 2. Within the following hours it gradually moved eastward north of the baseline, whereas the low-level cold air was blocked by the Alps. This is consistent with the manual θ_e analysis and regional model predictions for the 700-hPa level, which are given in Volkert et al. (1992, Figs. 6 and 2, respectively).

The frontal progression during IOPs B and D is given in Figs. 3 and 4 with the same isoline increment. In all three cases the front crossed most of the area of dense observations within less than 9 hours. The mean direction of the progression varied from eastward (IOP-A) over southeastward (IOP-B) to mainly southward (IOP-D). Conventionally analyzed surface front isochrones for these cases exhibit the same characteristics; see Hoinka and Volkert (1992, Figs. 3 and 4).

In Figs. 2–4, regions of negative absolute vorticity are indicated with the dashed contour. It appears that this zone is a persistent feature of the Alpine flow, as it is diagnosed for 10 of the 12 independent data samples irrespective of the particular front position. For a closer inspection of this negative anomaly IOP-B is used. The complete structures of the absolute vorticity and the horizontal flow field are exemplified for IOP-B, 1500 UTC in Fig. 5. The dash–dotted line encircles the region where the potential vorticity is negative; it nearly coincides with the line of vanishing absolute vorticity.

West–east and south–north vertical sections through the negative anomalies are presented in Figs. 6 and 7. The zero absolute vorticity contour within the θ_e distribution shows that the anomaly extends throughout the lower half of the troposphere in the warm air ahead of the cold front (Fig. 6). Furthermore, it is apparent that the negative potential vorticity is associated with negative absolute vorticity but positive static stability (Fig. 7).

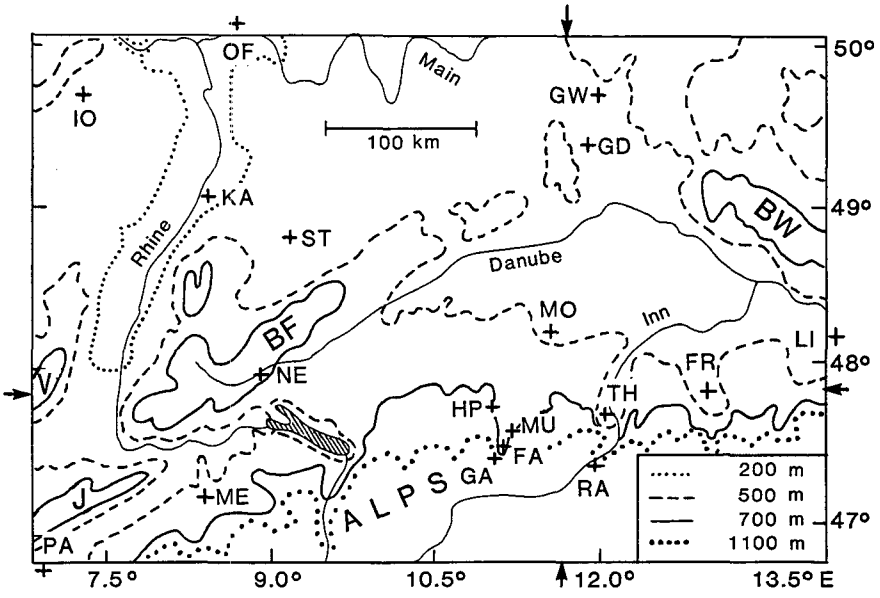

FIG. 1. Central part of the north Alpine foreland showing major rivers, smaller ranges (BF: Black Forest; BW: Bayerischer Wald; J: Jura; V: Vosges) and sounding stations of the German Front Experiment 1987 (crosses). The selected orographic contours were obtained from heights averaged over 10 km by 7 km areas. The arrows indicate the positions of the cross sections in Figs. 6 and 7. Two-letter codes designate the sounding stations: FA—Farchant; FR—Freilassing; GA—Garmisch; GD—Gärmersdorf; GW—Grafenwöhr; HP—Hohenpeißenberg; IO—Idar-Oberstein; KA—Karlsruhe; LI—Linz; ME—Merenschwand; MO—München-Oberschleißheim; MU—Murnau; NE—Neuhausen ob Eck; OF—Offenbach; PA—Payerne; RA—Radfeld; ST—Stuttgart; TH—Thalreit.

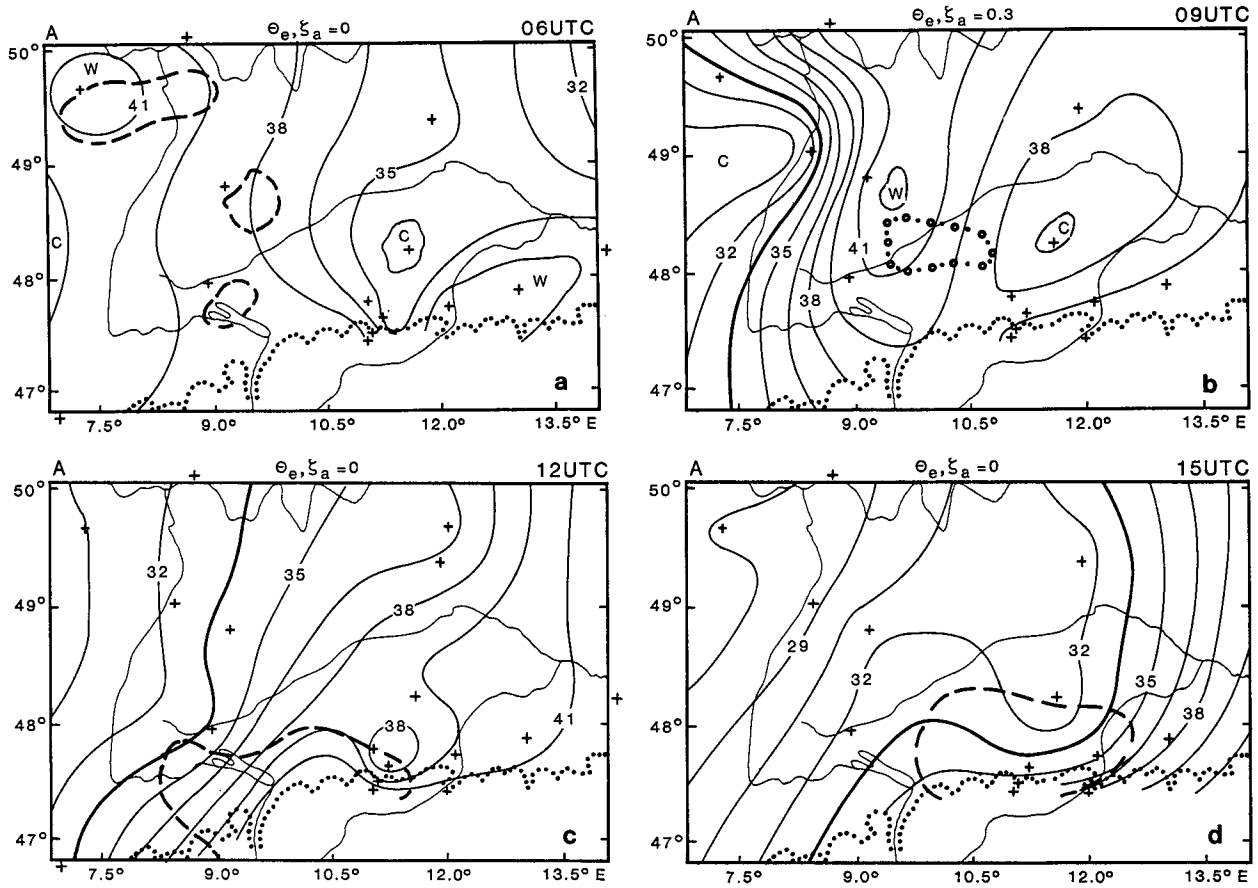

FIG. 2. The equivalent potential temperature at 0600, 0900, 1200, and 1500 UTC for IOP-A at 850 hPa and outside the Alpine area. The 33.5°C isotherm is pronounced to indicate an intrusion of cool and dry air from the west. The dashed contours enclose regions where the absolute vorticity is negative, and the dotted contour shows where it is below 0.3×10^{-4} s^{-1} (0900 UTC). The crosses denote available radiosonde stations (cf. also Fig. 1).

c. *Conclusions from the analyses*

It is clear from these analyses that the horizontal flow is relatively unaffected by the passage of the front. This is in contrast to the thermodynamic structure that undergoes the more or less classical airmass modification. It would appear that the prefrontal environment is one that produces a strong and relatively unsheared airflow parallel to both the Alpine chain and the approaching front. This is not surprising and presumably is the flow of warm, moist subtropical air, sometimes referred to as the warm conveyor belt. What is perhaps more surprising is that the airflow in its interaction with the Alps produces strong mesoscale flow structure in the Alpine foreland region. As in Kurz (1990), who evaluated the 1200 UTC radiosoundings of IOPs A and B for entire central Europe, we have drawn attention to the presence of strong anticyclonic vorticity to the north of the Alps, which is often of an amplitude such that absolute vorticity is negative. An analysis of the complete German Front Experiment radiosonde data revealed that this shear zone is largely ageostrophic and persists for several hours. As it is ageostrophic, such a zone of negative absolute vorticity cannot necessarily be regarded as implying the presence of inertial instability. The negative vorticity anomaly is strongest in the lower troposphere with a maximum intensity at around 850 hPa. The shear zone also appears to have negative potential vorticity.

The existence of these large anomalies of PV suggests that the role of diabatic or frictional processes may be important. The upstream flow, which has positive potential vorticity, can only have its PV changed by such processes. These results persuade us that it is important to quantify the mesoscale characteristics of the flow parallel to the Alps for the simpler case without the front and for idealized situations with surface friction neglected as well as included.

3. Mountain orography

The representation of the Alpine orography in theoretical and numerical models is an extremely difficult problem. Here we use two radically different solutions.

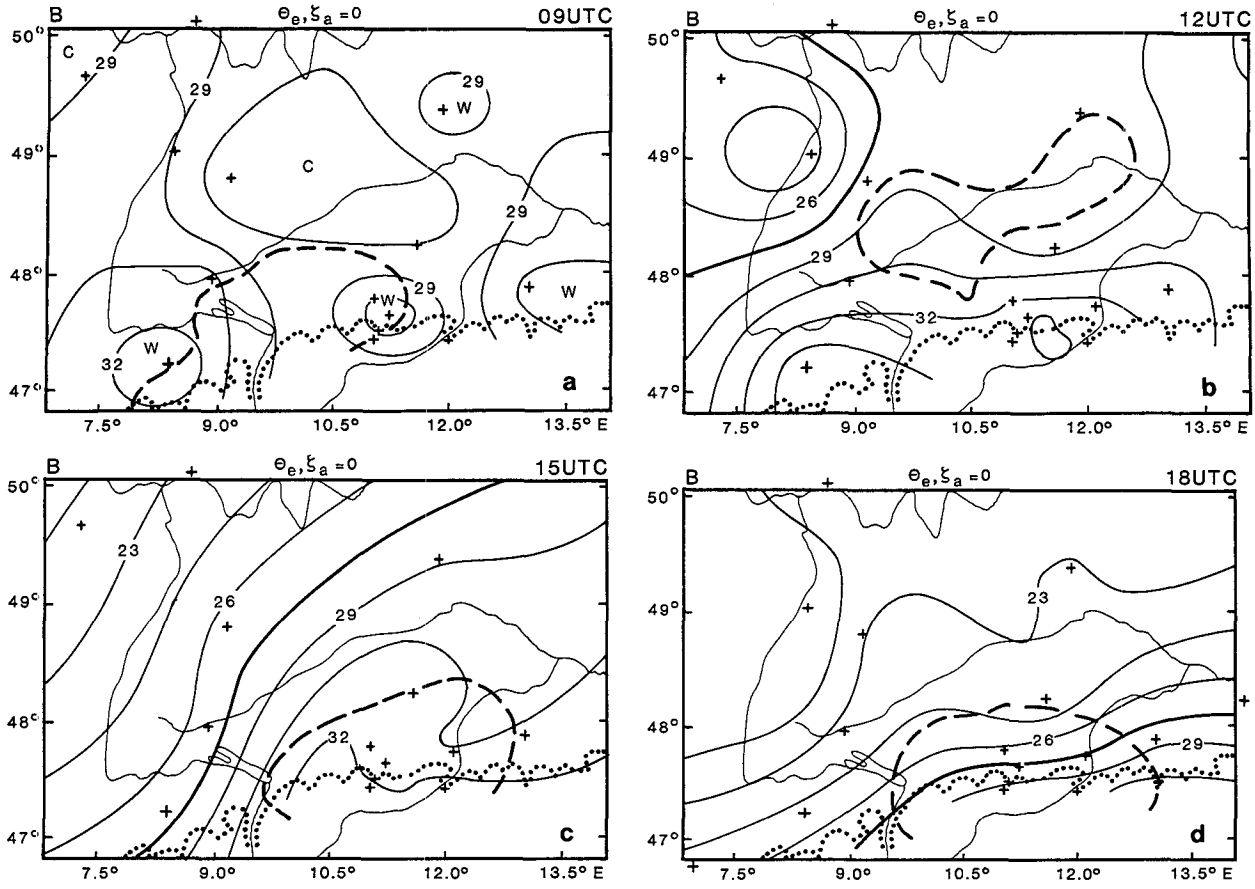

FIG. 3. The equivalent potential temperature at 0900, 1200, 1500, and 1800 UTC for IOP-B at 850 hPa and outside the Alpine area. The 27.5°C isotherm is pronounced to indicate an intrusion of cool and dry air from the west. The dashed contours enclose the regions where the absolute vorticity is negative. The crosses denote available radiosonde stations (cf. also Fig. 1).

The first is to produce a highly idealized and smooth orography, which has only a limited similarity to the Alps. It is useful, however, in allowing idealized theoretical models, such as the linear steady-state model, to be solved, giving an insight to the important gross features of the flow. The small-scale detail will of course be missing from such solutions. The second orography is used in a full nonlinear numerical simulation and is as detailed as the resolution used in the numerical model will allow. We refer to this as the "realistic" orography. The horizontal grid length of that simulation is 25 km, and the orography is derived as a smoothed version of an Alpine orographic dataset with about a 5-km resolution.

The idealized orography has been devised with the approximate dimensions of the Alps. For convenience the orientation of this mountain is taken to be east–west with a mean flow that is a constant westerly. The results are, of course, relevant to any mountain orientation as long as the flow is parallel to the orography. The idealized orography has north–south and east–west symmetry. The following is its mathematical form:

$$h = \max\left(\frac{h_m + h_c}{\langle 1 + \{[\max(|x| - x_m, 0)]^2 + y^2\}/b^2\rangle^2} - h_c, 0\right). \quad (4)$$

For convenience the mountain is centered at the coordinate system origin, and the x axis points along the mountain major axis. Here h_m is the maximum height of the mountain, h_c is the cutoff height that determines the horizontal location at which the orography becomes zero, x_m is the half-length of the ridge section, and b is the horizontal scale over which the mountain elevation diminishes. This form for the orography is composed of two semicircular ends separated by a ridge section. If x_m were to be zero, then we would recover a circular obstacle. A novel feature is that the mountain elevation is made zero at a finite distance from the peak; this is not true of the classical mountains, such as the Witch of Agnesi, or bell-shaped orography, which have zero elevation only at an infinite distance from the mountain. The consequence of this choice is that the slope

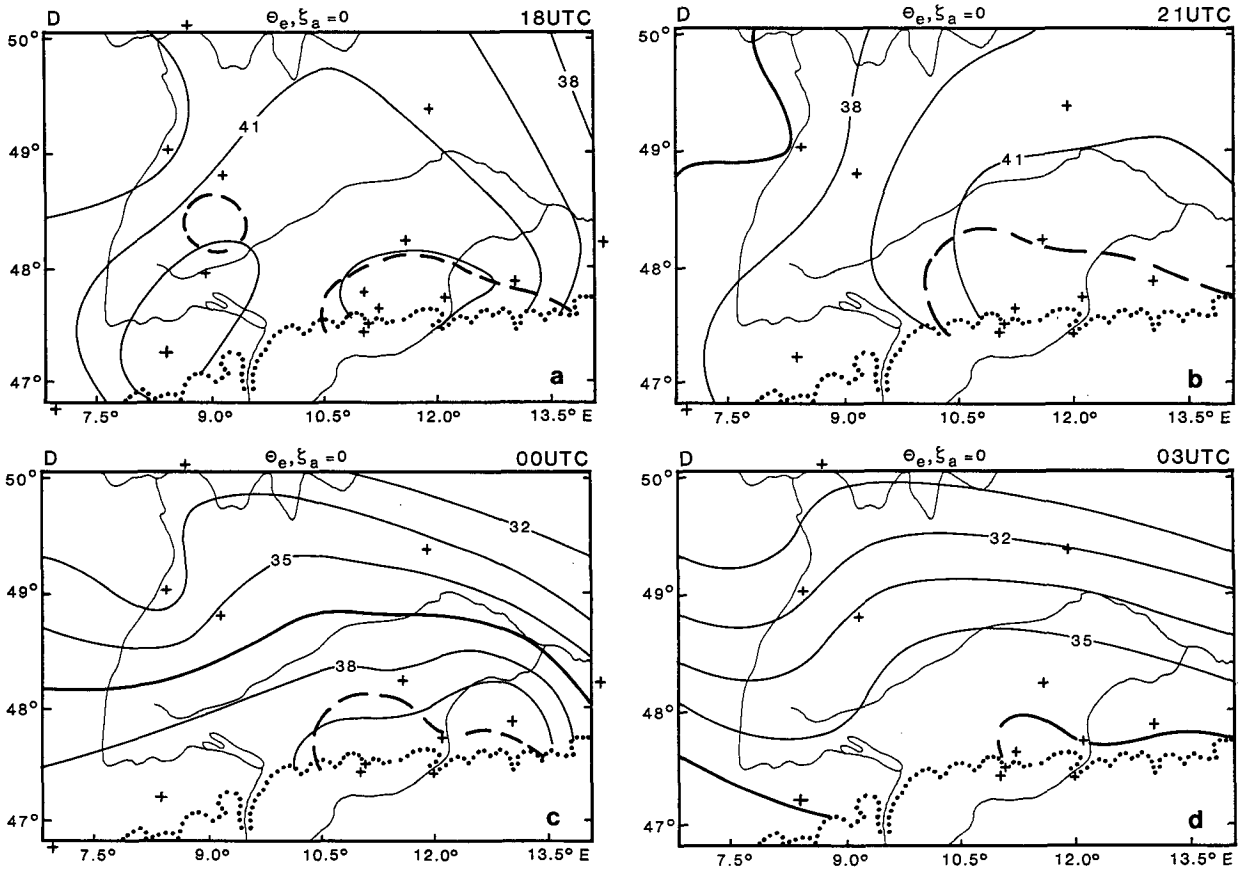

FIG. 4. The equivalent potential temperature at 1800, 2100, 0000, and 0300 UTC for IOP-D at 850 hPa and outside the Alpine area. The 36.5°C isotherm is pronounced to indicate an intrusion of cool and dry air from the northwest. The dashed contours enclose regions where the absolute vorticity is negative. The crosses denote available radiosonde stations (cf. also Fig. 1).

of the mountain changes discontinuously at the surrounding plain in accord with the actual Alpine orography. The curved western end of the Alps is not included in this idealized orography but, as we will comment later, it may play a significant role in the details of the observed mesoscale flow.

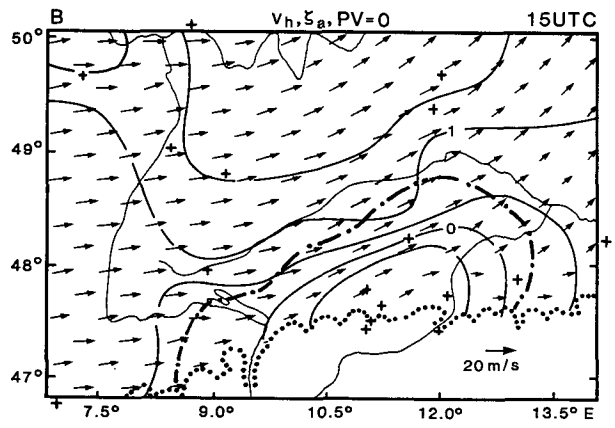

FIG. 5. The distribution of absolute vorticity and horizontal wind vectors at 850 hPa at 1500 UTC for IOP-B (increment of vorticity: 0.5×10^{-4} s^{-1}). The dash–dotted line encloses the region of negative potential vorticity. The crosses denote available radiosonde stations (cf. also Fig. 1).

4. Linear steady-state model

A relatively tractable and often illuminating technique when considering mountain flows is to consider a uniform airstream impinging on the mountain and to examine the steady-state but linear response to that airflow. We are encouraged to make such calculations here as the upstream flow in the observations is relatively unsheared and because the flow in the vicinity of the mountain is persistent and largely ageostrophic. The model has large limitations such as its linearity and its neglect of frictional effects, but we feel it is an important beginning point in the understanding of the dynamics of the flow. Here only the method is sketched; it has been described for other cases in more detail by Smith (1980). We will focus on the vorticity, which has not previously been discussed in this connection. Dynamical insight can be gained from the linear model for use in understanding the flow both in the observations and in nonlinear numerical simulations.

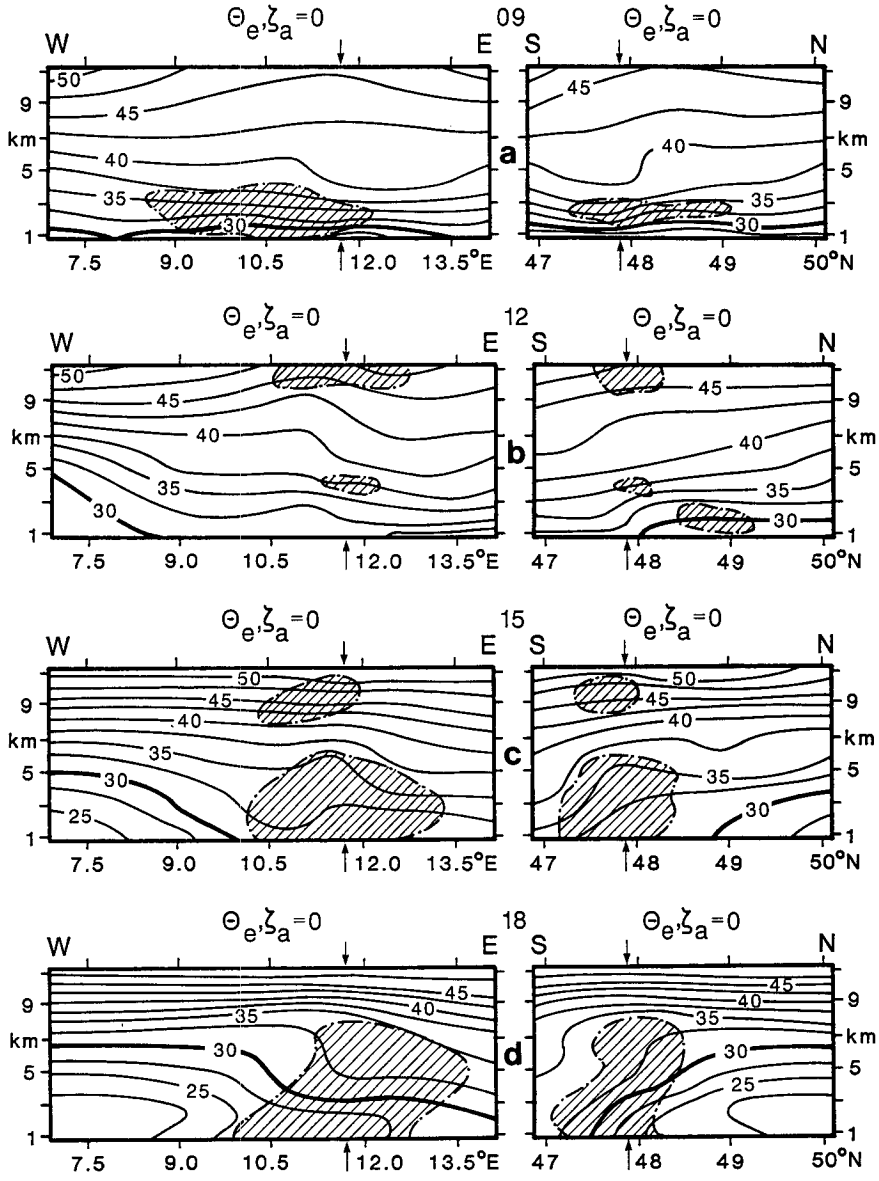

FIG. 6. West–east (at 47.9°N) and south–north (11.7°E) sections of equivalent potential temperature at 0900, 1200, 1500, and 1800 UTC for IOP-B. Regions of negative absolute vorticity are hatched. The arrows indicate the line where both sections intersect (cf. also Fig. 1).

For adiabatic frictionless flow the potential vorticity should be conserved. For flow impinging on the mountain considered in the linear model the potential vorticity is a constant given by $fN^2\theta_0/g$ as we are dealing with constant static stability and mean flow. The potential vorticity is a quadratic quantity that in this case can be decomposed into a part due to the mean flow, as given above, a part due to products of the mountain disturbance and the mean flow (first order), and a part that involves products of terms involving the mountain flow (second order). The linear approximation of the PV only involves the mean flow and the first-order terms. From the linear equations, discussed in the next subsection, it is clear that the perturbed static stability, $\partial\theta'/\partial z$, and relative vorticity, ζ_{rel}, are closely related via the equation

$$\frac{\partial\theta'}{\partial z} = -\frac{N^2\theta_0}{fg}\,\zeta_{\text{rel}}. \tag{5}$$

This constraint on the static stability is absent in the nonrotating case. In an anticyclonic region the static stability is therefore large, for example. This relationship between the disturbance static stability and vor-

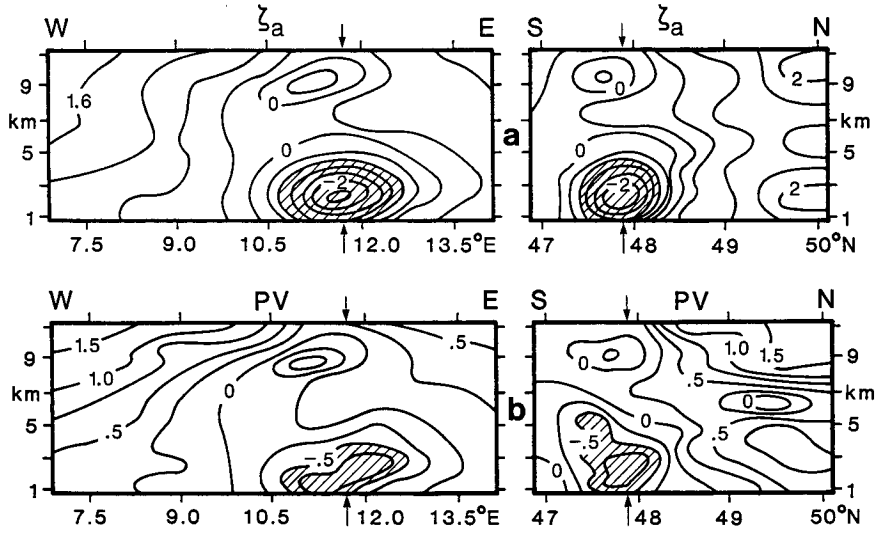

FIG. 7. Cross sections at 1500 UTC as in Fig. 6 but for (a) absolute vorticity (region with values below -0.8×10^{-4} s^{-1} is hatched) and (b) potential vorticity (region with values below -0.5 PVU is hatched; 1 PVU = 10^{-6} m^2 s^{-1} K kg^{-1}).

ticity means that the first-order terms in the expression for the potential vorticity add up to zero. Hence, the linear model conserves potential vorticity to first order, and there are no errors introduced by lack of PV conservation. Of course, the nonlinear terms will produce a second-order correction to the PV. The flow is strongly ageostrophic, which makes this constraint imposed on the static stability due the uniformity of the potential vorticity of some interest.

a. Mountain wave theory

The linear steady-state Boussinesq momentum equations with no friction and the thermodynamic equation giving the conservation of potential temperature are used with a constant mean flow, U, in the x direction. For a Fourier wave component, for any variable X, of the form:

$$X' = X_0 e^{i(kx+ly+mz)}, \tag{6}$$

these linear equations can be written in terms of the vertical displacement, η, of an air parcel defined in terms of the vertical velocity, w, by $w = U\partial\eta/\partial x$. The vertical wavenumber, m, must satisfy the following relationship if the above are to be solutions of the equations:

$$m^2 = \frac{N^2 - k^2U^2}{k^2U^2 - f^2}(k^2 + l^2). \tag{7}$$

The linear model can be solved numerically for any shape of (periodic) mountain, $h(x, y)$, by noting that at the surface, defined by $z = 0$ in the linear model, $\eta = h$. Above the surface each wave component must have the following form so as to propagate energy upwards:

$$X' = X(z = 0)e^{i\mathrm{sgn}(k)mz}. \tag{8}$$

The solution can be found by making a Fourier decomposition of the mountain shape [this gives $\eta(z = 0)$] and then multiplying by the vertical structure factor and making a Fourier combination of all the modes. Further details of the equations and the solution method are given by Smith (1980) for the nonrotating case. For most of the results shown here the domain in which the equations are solved is 6000 km $\times$ 3000 km with 600 $\times$ 300 grid points, the larger number being in the mean flow direction.

A dynamical understanding of the flow characteristics relies on an understanding of the component inertia–gravity waves of which the solution comprises. A key parameter is the vertical wavenumber. It is real, corresponding to upward propagation, for horizontal wavenumbers k in the range from f/U to N/U. At the inertia wave limit, $k = f/U$, and the vertical wavelength is zero while at the gravity wave limit, $k = N/U$, and the vertical wavelength is infinite. Outside this range the waves are evanescent, that is, damped in the vertical. A way of interpreting the consequences of this behavior is by looking at the group velocity. Near the inertia wave limit the energy propagation is almost entirely horizontal, while near the gravity wave limit the energy propagates almost entirely vertically. Also, the energy propagation in the direction normal to the mean flow, y, is N/f times greater near the inertia wave limit than near the gravity wave limit.

Aspects of the inertia wave limit have been discussed by Eliassen (1968), who comments on the appearance

downstream of mesoscale mountains of an undamped train of horizontal inertia waves with wavelength $2\pi U/f$. It should be noted, however, that the exactly horizontal inertia wave is only one component of the wave field, and when the horizontal wavelength is smaller than the above limit the waves propagate energy predominantly downstream but with a finite vertical propagation also. Over small-scale mountains there is almost no contribution to the flow from the inertia-dominated waves, and the flow can be understood in terms of almost vertically propagating gravity waves. The inertia waves appear in the horizontal velocity fields but do not have a signature in pressure. Consequently, they are entirely ageostrophic. They are not, however, purely horizontal structures. To maintain the uniform potential vorticity the anticyclonic (cyclonic) gyres have an increased (decreased) static stability.

The results to be shown are applicable for particular values of the governing nondimensional parameters of the problem. These are

1) basic scalings: vertical, U/N; horizontal, L; velocity, U

2) flow parameters in the nondimensional linear equations: $F = U/(NL)$; Rossby number $\mathrm{Ro} = U/(fL)$

3) nondimensional orographic parameters: Froude number $\mathrm{F_r} = U/(Nh_m)$; x_m/b; $U/(Nh_c)$.

Here the horizontal scale, L, is associated with the mountain horizontal scale and can be chosen to be a suitable combination of b and x_m. The results to be shown here have $\mathrm{F_r} = 1$, $U/(Nh_c) = 5$, and $x_m/b = 3.6$; if $L = b$ then $F = 0.04$ and $\mathrm{Ro} = 4$, or if $L = x_m$ then $F = 0.01$ and $\mathrm{Ro} = 1.1$. These values are consistent with a mountain that has $h_m = 2.5$ km, $h_c = 500$ m, $x_m = 225$ km, $b = 63$ km, and a flow with $U = 25$ m s^{-1}, $N = 0.01$ s^{-1}, $f = 0.0001$ s^{-1}, giving a typical vertical scale of $U/N = 2.5$ km. Note that $\mathrm{F_r}$ can be interpreted as the inverse of the nondimensional mountain height.

Smith (1980) comments on the validity of the linear model in the nonrotating case; we use these criteria as a guide to those when rotation is included. The limits of validity of the linear model, in the case of a circular mountain with no rotation, are associated with the following aspects of the flow:

- flow stagnation in the mean flow direction if $\mathrm{F_r} \leq 0.33$
- lateral (y direction) deflection of the flow greater than the mountain width if $\mathrm{F_r} < 1$
- static stability is negative if $\mathrm{F_r} \leq 2$.

It is clear therefore that the most restrictive condition on the linear theory is associated with the static stability. For the orography and mean flow used here the static stability is negative locally as the Froude number is less than 2. The region of breakdown of the linear model is downstream of the mountain—that is, to the east of the "Alps"—and so we regard the results as having validity in the region north of the orography where our particular interest lies. Also, the breakdown region is confined to the surface layer. The model has been used for smaller h_m; consequently, larger $\mathrm{F_r}$, and the mesoscale flow structure is relatively unaffected. In fact, in zones of anticyclonic vorticity, such as we are examining, the static stability anomaly is positive, so the linear model is valid there.

b. Flow structure

As noted by Smith (1982) for flow impinging on a mesoscale mountain range that exhibits symmetry in the direction perpendicular to the flow (i.e., north–south in this case), the pressure field, vertical velocity, and displacement are symmetrical, but the flow field is not in the presence of the Coriolis force. Here we find that the flow north of the "Alps" is stronger than that to the south, with flow from the western end towards the eastern end, Fig. 8a. The flow to the south of the mountain is generally weaker and less simple. There is faster flow to the north compared to the south of the mountain. Of some importance here is the fact that the flow from east of about one-third the distance along the obstacle is towards the mountain. The general anticyclonic nature of the flow is clear.

The vorticity pattern is symmetrical about the west–east central axis of the mountain even though the flow

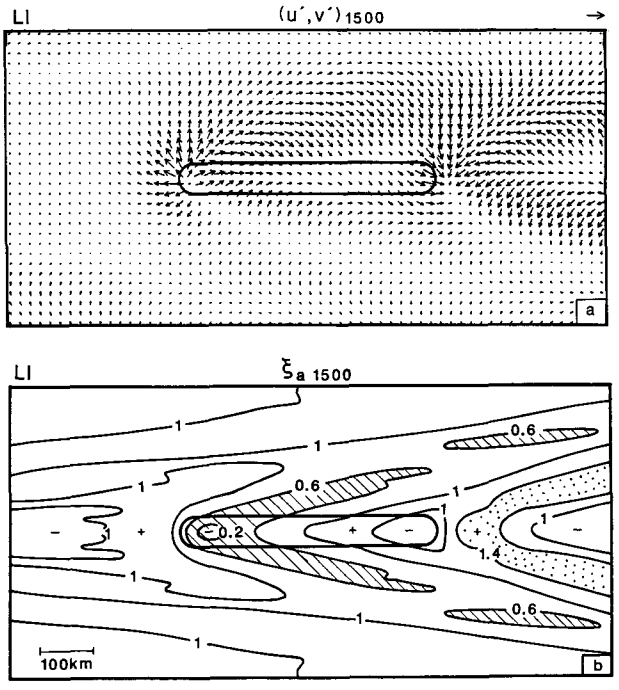

FIG. 8. (a) Horizontal perturbation flow vectors (unit vector: 10 m s^{-1}) and (b) the absolute vorticity divided by f (contour interval 0.4; regions below 0.6 are dashed and above 1.4 dotted) at $z = 1500$ m in the linear steady-state model (LI). In this and subsequent figures the mountain outline appropriate for the given height is superimposed.

is not. This is because in the linear model the only generation of vertical vorticity is due to the stretching of planetary vorticity. As the vertical velocity, and hence stretching, is symmetrical then so is the vorticity. (Note that as a consequence in a nonrotating flow there is trivially zero vertical vorticity.) Horizontal vorticity is generated by the baroclinic mechanism. The nonlinear production of vertical vorticity by the tilting of horizontal vorticity is, of course, absent here. This is probably a less serious error on the scales being considered here than it is for small-scale mountains. This mechanism has been postulated by Smolarkiewicz and Rotunno (1989) as the main reason for vortices downstream of mountains at low Froude number. At $z = 0$ there is strong anticyclonic vorticity downstream of the mountain but with little vorticity north or south of the mountain. At upper levels the vorticity has a v-shaped configuration with anticyclonic vorticity streaming from the western end and cyclonic vorticity from the eastern end of the mountain, Fig. 8b. In the lower troposphere to the north of the "Alps" there is a line of anticyclonic vorticity. This line has a width of about 100 km and is oriented south-west-north-east. Given the limitations of the model this line of anticyclonic vorticity is located in a similar position to that shown in the prefrontal observations.

There is a characteristic v-shaped pattern of the displacement and the pressure fields associated with the waves in the horizontal plane and a changing tilt of that pattern with height (not shown). In the vertical plane there is also a v-shaped pattern of mountain waves, and this can be understood in terms of the group velocity; see Smith (1980). From the equation for the ratio of c_{gz} and c_{gy} and for a mountain wave with $(k^2 + l^2) = 1/b^2$ the slope of the fields in the y–z plane should be approximately $U/(Nb) = 0.04$. This slope of 1 in 25 is characteristic of the fields in the vicinity of the mountain. In a meridional–vertical cross section the region of anticyclonic vorticity that slopes upward and northward from the mountain is accompanied by descent (and high static stability, Fig. 9). Farther aloft there is a weaker zone of sloping cyclonic vorticity accompanied by ascent. This vertical motion pattern could be of some importance in coupling with the cross-frontal circulation of an approaching front. For non-frontal situations but when the mean flow is along the Alpine axis, the upper-level ascent north of the Alps should be accompanied by lower-level descent, thus suggesting the suppression of convection from near the surface but an enhancement of midlevel clouds.

c. *Conclusions from linear model*

The linear steady-state model has shown the general characteristics of the flow in the vicinity of an idealized obstacle chosen to represent the Alps. The results indicate that there is a zone north (and south) of the orography with anticyclonic vorticity. The constraint

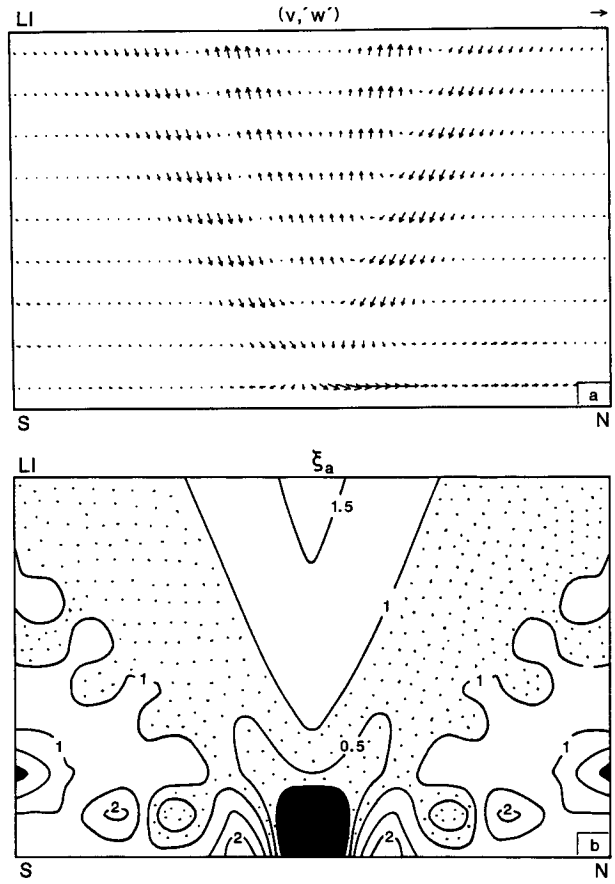

FIG. 9. A S–N cross section at the midpoint of the mountain chain ($x = 0$) showing (a) velocity vectors (v', w') (unit vector: 10 m s^{-1} with the vertical velocity component multiplied by 100), and (b) the absolute vorticity divided by f (contour interval: 0.5; regions of negative values are blackened; range between 0 and 1 is dotted). The domain area is 600 km × 4.5 km.

of conservation of potential vorticity requires that the absolute vorticity remain positive in such a region where the flow is stably stratified.

To explain the observed negative absolute vorticity we are therefore left with either nonlinear or frictional processes. Nonlinear dynamics cannot modify the potential vorticity, although in principle such effects could produce negative absolute vorticity and static stability, leaving the potential vorticity positive. This seems unlikely and, in any case, would not account for the coexistence of negative absolute and potential vorticity. We can therefore postulate that frictional processes must be responsible for the vorticity and potential vorticity structure seen in the observational analysis presented in section 2. This hypothesis will be explored in the next section.

5. Nonlinear model simulations

The steady nonlinear flow past the obstacle is now considered using a three-dimensional time-dependent

numerical model. This allows one to assess both nonlinear effects and the role of frictional processes. These simulations use the Heimann (1990) hydrostatic mesoscale model, and a detailed description of the model can be found in that paper. In the simulations the mountain is introduced over the first hour in such a way that the isentropes are essentially horizontal at the end of this period and therefore intersect the mountainside. This model can be run with a (sophisticated) 1½-order closure frictional boundary-layer representation based on the explicit computation of the turbulent kinetic energy, E. Horizontal and vertical mixing coefficients are computed from E and are used in the computation of turbulent fluxes of heat and momentum. In these frictional simulations there is a no-slip lower boundary with vertical profiles derived by assuming a constant flux surface layer. The model is initialized with horizontally homogeneous profiles of all variables. These have been derived previously from a one-dimensional column integration to a statistically steady state. For simulations without friction the turbulent mixing is set to zero, and free-slip boundary conditions are used.

Here runs with a constant flow past the idealized orography given previously and past a realistic Alpine orography will be described. Also, for the idealized orography simulations will be described that have no explicit friction and have the complete model turbulence scheme with a no-slip lower boundary condition. The "frictionless" case is an attempt to make the nonlinear model as similar to the linear one as possible.

As discussed in the Introduction, with friction the numerical model has a boundary layer in which the potential vorticity is no longer conserved. The effect friction has on the upstream boundary layer is to produce a layer with small PV, but which is horizontally homogeneous. As the air flows past and over the Alps there is an *extra* forcing of PV anomalies, which can be visualized as in Fig. 10 if one considers a level of, say, 1.5 km about halfway up the mountain. At this level the westerly flow past the Alps suffers a frictional force directed towards the west where it impinges on the Alps but no frictional force to north and south of the orography. Hence, there is a frictional force curl directed downward north of the Alps and upward south of the Alps. Therefore, there is a negative potential vorticity tendency north of the Alps, and a positive one to the south. Another way to visualize this process is to imagine that as the mountain range slopes upward the boundary layer is tilted such that it acquires a slope. The consequent horizontal velocity gradient, as opposed to the vertical one in a horizontal boundary layer, contributes to anticyclonic vorticity, and potential vorticity, north of the Alps and the opposite to the south. This physical picture of the additional mountain PV forcing is important in making the distinction between dynamical processes responsible for the production of anticyclonic vorticity and the physical processes

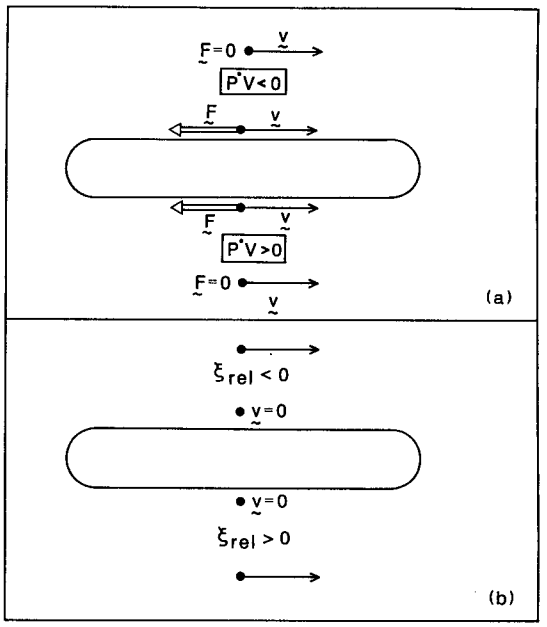

FIG. 10. Explanatory sketch of (a) the time rate of change of potential vorticity due to the frictional force F and (b) the horizontal flow and relative vertical vorticity that results from that frictional process. Both figures refer to a level of about 1500 m, which is above the boundary layer away from the mountain but intersects the mountain sides. The solid line indicates the idealized mountain orography at this level. The flow away from the mountain is unaffected by friction, whereas on the mountainside the flow is zero. The PV forcing shown here is an additional one due to the presence of the mountain and its sloping boundary layer.

required to change the potential vorticity. For example, the linear steady-state model has anticyclonic vorticity north of the Alps, but this is not accompanied by a reduction in the potential vorticity.

a. Idealized orography

The numerical model was run with the idealized symmetrical orography oriented west–east as used in the linear model. The horizontal grid length is 25 km, and the domain is 2000 km × 1000 km × 9 km. The vertical grid is staggered with 20 levels in total but with greatest resolution in the boundary layer; a damping sponge layer is used in the upper layers of the model. The initial conditions are as in the linear model with $U = 25$ m s^{-1} and a constant static stability of 3.5 K km^{-1}. Thus, the simulation has the same parameters, such as Froude number, as in the linear model. The mountain was slowly introduced over the first hour of the simulation, and the model was run for periods up to 18 h in an attempt to reach a steady state.

In the first set of simulations the model is run with no explicit friction except the upper damping layer. Here results from 8 h are shown, after which time the flow is essentially in a steady state. In Figs. 11, 12, and 13 we compare the frictionless simulation with the lin-

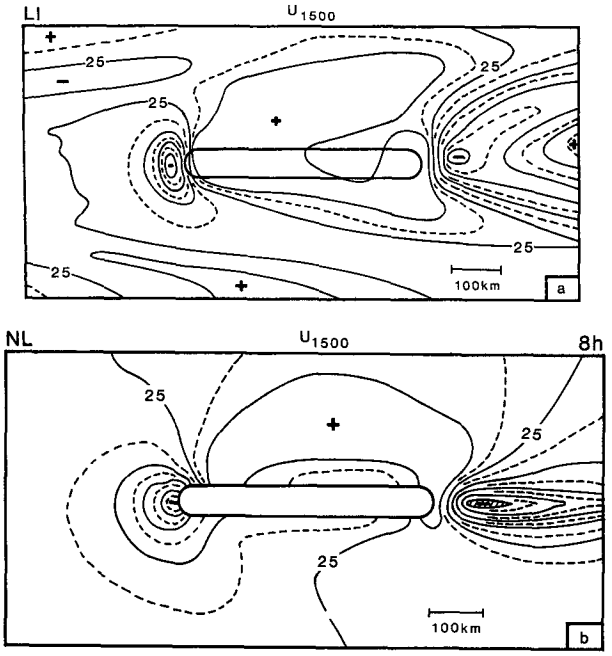

FIG. 11. Zonal velocity at the 1500-m level around the idealized mountain range (thick contour) as calculated by (a) the linear model and by (b) the inviscid nonlinear (NL) calculations 8 h after initialization. Bold isolines differ by 2 m s^{-1}; intermediate contours are dashed; regions with values less than 17 m s^{-1} are hatched.

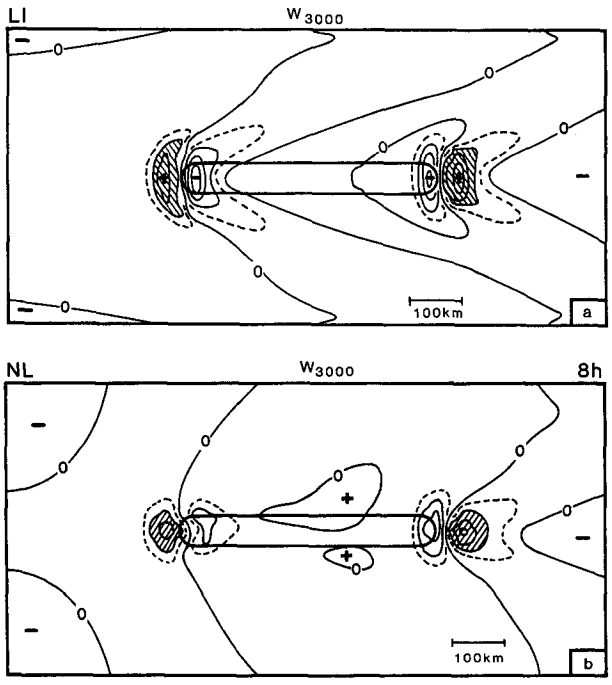

FIG. 12. As in Fig. 11 but for the vertical velocity at 3000 m (thick contour indicates the location of the 1500-m height contour of the orography). Bold isolines differ by 0.2 m s^{-1}; intermediate levels are dashed; regions with values above 0.2 m s^{-1} are hatched.

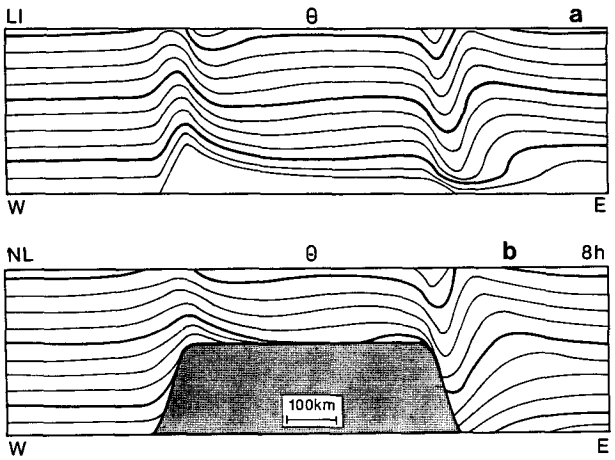

FIG. 13. A W–E cross section along the central axis of the mountain chain ($y = 0$) showing potential temperature for (a) the linear model and (b) the nonlinear calculations 8 h after initialization. Bold isolines differ by 6 K; thin ones by 1.5 K. The domain area is 1150 km × 4.5 km.

ear model. It is apparent that in most respects the linear model gives flow similar to the nonlinear model. One region that is significantly different at 4 h, but more particularly after 8 h, is that immediately downstream of the mountain. The numerical model produces a much more retarded flow, with a minimum near the surface, than does the linear solution. One could plausibly suppose that this is due to nonlinear effects associated with the large hydrostatic gravity wave on the downstream downslope of the mountain. However, if we diagnose the numerical model prediction of potential vorticity a substantial nonconservation is found precisely in this region (see Fig. 14). This nonconservation is due to the implicit friction caused by the finite-differencing scheme. We have tried with an entirely different and more accurate horizontal and vertical differencing based on a spline method, and the results for PV are only slightly improved. This type of numerical behavior has been noted previously by Volkert and Bishop (1990) in the context of an Eady wave simulation in which PV conservation is broken as the front becomes intense at the surface. We believe that this is a serious limitation of the numerical model results, which would be typical of any such model that does not explicitly conserve PV. There is some hope that numerical models based on isentropic vertical coordinates may be able to have a differencing scheme that conserves PV; see for example, Mattocks and Bleck (1986). However, such models have not yet been tried on the extremely disturbed mountain flows being discussed here.

In the second set of simulations the numerical model has been run with a no-slip lower boundary and a detailed boundary-layer scheme involving prediction of the turbulent kinetic energy. Fields are again shown at 8 h after initiation by which time the flow is about

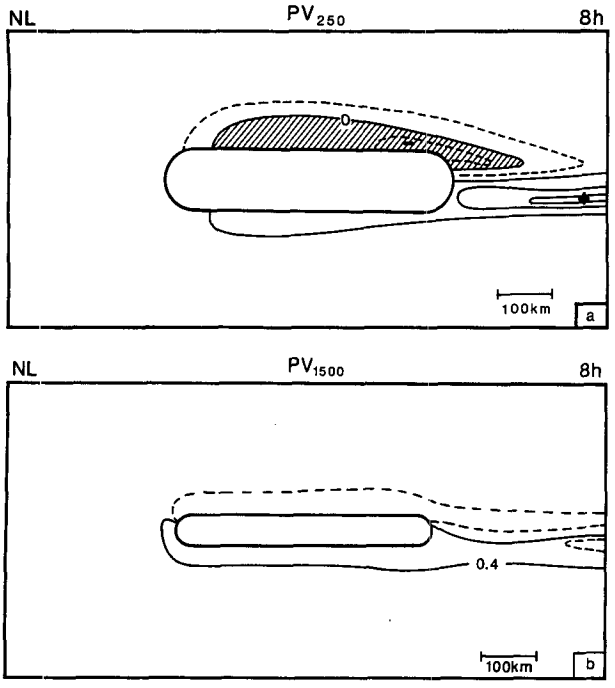

FIG. 14. Horizontal section of potential vorticity after 8 h of the nonlinear frictionless calculation at (a) 250 m and (b) 1500 m. Bold isolines differ by 0.4 PVU; intermediate levels are dashed; regions of negative values are hatched.

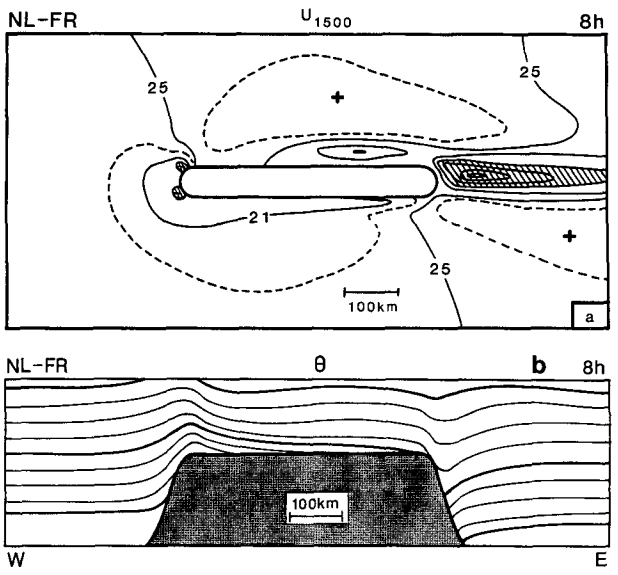

FIG. 15. Results of the nonlinear model with friction included (NL-FR) 8 h after initialization: (a) horizontal section of the zonal velocity (cf. Fig. 11, but note that the contour intervals are not the same) and (b) W–E cross section ($y = 0$) of potential temperature (cf. Fig. 13).

steady. In Fig. 15a we show the zonal velocity and in Fig. 15b, the potential temperature vertical section along the axis of the obstacle to compare with those in the frictionless simulations (cf. Figs. 11 and 13, respectively). It can be seen that the major differences due to friction in the zonal flow is in the region immediately downstream of the mountain where the flow is very strongly retarded. This is, we believe, due to a strong negative anomaly of potential vorticity in that region (see further comments on this aspect in the next paragraph). The other difference is the reduction in the amplitude of the hydrostatic wave downstream of the mountain apparent in the W–E vertical section.

The nonlinear simulations show, in Fig. 16, a zone to the north of the mountain in which the potential vorticity is substantially negative. This feature in the PV has similarities to that in the observations, but the PV anomaly is located rather closer to the mountainside in the simulations as compared with the observations. We believe that this is the basic explanation of that structure in the observations. It is also apparent from Fig. 16 that these PV anomalies are large at low and middle levels downstream of the mountain. This is reminiscent of the frictionless simulation shown in Fig. 14 but with a much larger magnitude in the case with friction. Apparently the model's implicit friction due to the numerical scheme gives PV anomalies that are similar in structure but smaller in amplitude to those produced by the realistic turbulent processes included in the case with explicit friction. It is now clear that a zone of strong flow retardation (by as much as 20 m s^{-1}) can be expected downstream of the "Alps" due to the anomalies in potential vorticity caused by

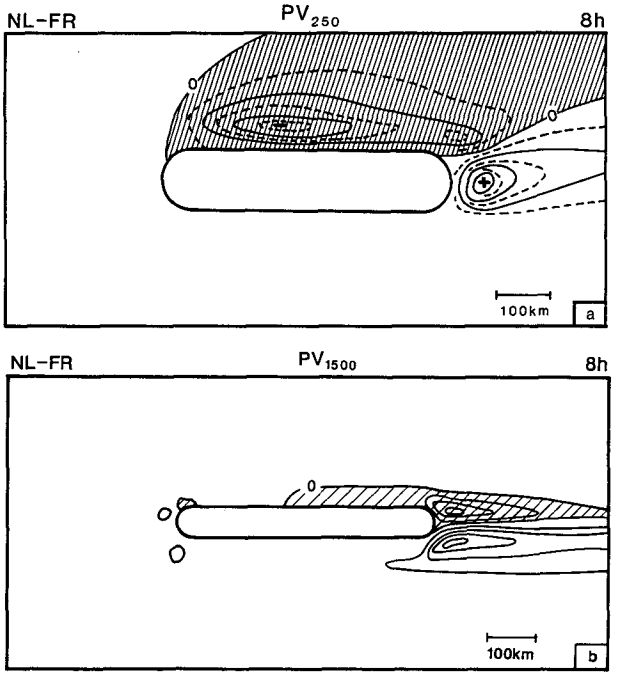

FIG. 16. Horizontal section of potential vorticity after 8 h of the nonlinear calculation with friction included at (a) 250 m and (b) 1500 m (cf. Fig. 14). Bold isolines differ by 0.4 PVU; intermediate levels are dashed; regions of negative values are hatched.

frictional processes. We are unaware of any observational evidence for such a zone, as there have been no detailed observations in that area. In fact, there is much stronger retardation downstream than upstream of the mountain (cf. in the linear frictionless case there is slightly stronger retardation upstream).

b. *Realistic orography*

The nonlinear model was run with a more realistic Alpine orography, as was used previously by Heimann (1990). The mean flow and stratification are kept constant, and the flow direction is taken to be 260°, which is along the central Alpine axis. The aim now is to use a realistic orography and physics but retain the simple flow to see whether the structures found in the observations are present. Hence, we take the frictional simulation with a resolution as for the idealized orography case. The simulation takes longer to establish a steady state due to the finer structure of the orography. Results are shown here after 18 h of simulation. It is worth noting that Dempsey (1989) simulated a westerly flow past a realistic Alpine orography but in the frictionless case.

The flow exhibits the same general characteristics as for the idealized orography. The general anticyclonic flow north of the Alps is apparent, and there is a region of negative potential and absolute vorticity north of the orography in the area of the observations; see Fig. 17. The role of the curved western end of the Alps is likely to be important in determining the location of the PV anomalies and their advection away from the mountainside. In the realistic orography case and in the observations the region of negative PV is located some 50 km north of the mountain. Changes in the mean flow wind direction would probably alter this location somewhat. For the idealized orography without the curved western end the region of negative PV is closer to the mountainside. A south–north vertical section through the PV minimum is given in Fig. 18. Potential and absolute vorticities are negative on the northern flank of the Alps; compare the right-hand side of Fig. 7 for a south–north section through the analyzed data. The boundary-layer vertical mixing coefficient K is shown in Fig. 18c; it is computed in the model as

$$K = 0.45l/\phi\sqrt{E} \tag{9}$$

from the mixing length l, the dimensionless profile function ϕ, and the turbulent kinetic energy E.

The mixing coefficient gives an indication of the location and depth of the boundary layer in the model. In particular, it can be seen that the boundary layer to the north of the Alps is about 1 km deep, and on the Alpine slope it acquires a significant horizontal extension. It is clear that this tilt of the boundary layer means that at, say 850 hPa, it extends horizontally from the Alpine slopes by as much as about 100 km to the north of the Alps. In contrast, to the south of the Alps the boundary layer appears more confined against the mountainside. This may be due to the influence of the hooked shape of the western end of the Alps.

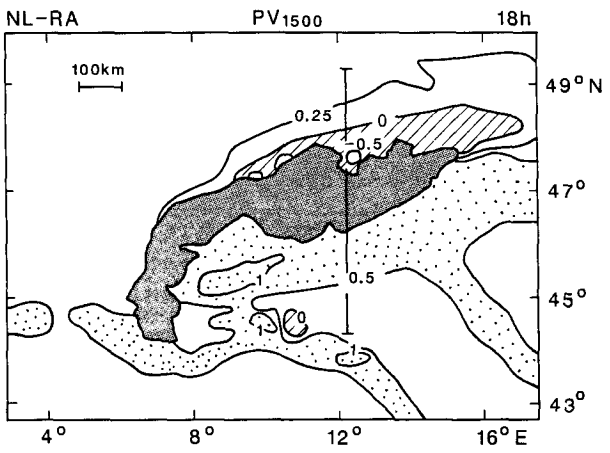

FIG. 17. Potential vorticity at the 1500-m level around a realistic Alpine orography (black) as calculated by the nonlinear model (NL-RA) with friction included 18 h after initialization. Regions of negative values are hatched, and areas with values above 0.5 PVU are dotted. The vertical bar indicates the position of the cross section displayed in Fig. 18.

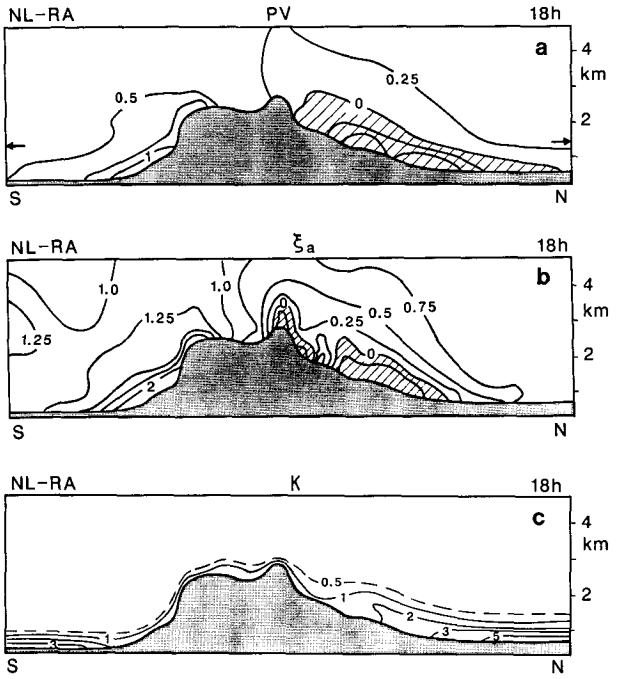

FIG. 18. South–north cross section across the realistic Alps (cf. Fig. 17) of (a) potential vorticity, (b) absolute vorticity divided by f, and (c) vertical exchange coefficient (unit: $m^2 s^{-1}$) as calculated by the nonlinear model with friction included. The horizontal arrows in (a) indicate the position of the horizontal section displayed in Fig. 17.

c. *Conclusions from the simulations*

The nonlinear model in the presence of the "realistic" orography exhibits a zone of anticyclonic vorticity reminiscent of the linear model. However, this zone has considerably lower vorticity if friction is included. This we attribute to a contribution by the friction associated with the sloping boundary layer on the mountain slope. A relatively modest slope to the boundary layer is capable of producing a large anticyclonic shear line in the northern Alpine foreland. The nonlinear model uses a rather complex boundary-layer scheme; however, it must be admitted that relatively little is known about boundary layers in such circumstances. Comparison of the results with and without friction show that there are two main areas in which the solutions differ. The first is the shear zone, to which we are drawing attention, north of the Alps observed in the German Front Experiment. The second is the strong zone of flow retardation downstream of the orography for which we have, as yet, no direct observational evidence.

6. Discussion

In this paper we have explored the dynamics of airflow that approaches the Alps from the west. This is typical of prefrontal flow in this region. The linear inviscid flow past the Alps has certain characteristic mesoscale structures. For example, the vorticity is anticyclonic both to the north and south of the Alps, and at midmountain height this zone extends away from the mountain in a wake pattern emanating from the western side of the Alps. The hydrostatic mountain wave pattern leads to regions of sloping ascent and descent on either side of the mountain. The linear model of the airflow conserves the linear approximation to the potential vorticity. Hence, the linear frictionless dynamics cannot account for the observations of negative PV in the northern Alpine foreland.

The role of friction is crucial in leading to the production of anomalies of PV lying to the north and south of the Alps; negative to the north and positive to the south. The vorticity pattern is modified by the frictional changes to the flow giving an enhancement of the anticyclonic vorticity north of the mountain and the existence of cyclonic vorticity to the south.

The mechanism of production of PV anomalies is attributed here to the existence of a sloping frictional boundary layer. The physical picture is strongly dependent on the retardation of the flow attached to the mountainside relative to the frictionless flow at levels above the boundary layer over the surrounding plain. The frictional effects are sufficient to make the absolute and potential vorticity negative north of the Alps. The significance of such a region of negative PV to any incoming front is interesting but not directly addressed here. One might have supposed that the frictional effects would be felt only in an extremely narrow zone immediately adjacent to the mountain. Both the observations and the nonlinear model show that this is not the case and that the region extends some 100 km north of the orography. The reason for this extension is, we believe, twofold. The first is the effect of the bowlike mountain wave emanating from the western side of the Alps; this leads to structures such as the zone of anticyclonic vorticity being located well to the north of the orography. The second is due to advection of this horizontal boundary layer away from the mountainside. This leads, in the realistic orography simulation, to the zone of negative PV streaming away from the Alps in a quasi-two-dimensional structure. This is in effect a shear line with negative PV.

Other regions of the flow past the Alps have mesoscale structure. To the south of the Alps the PV is increased, and for the realistic orography there is a localized region of PV anomaly in the Po Valley centered near Milan. This may be important in enhancing any upper-level forcing of lee cyclogenesis by a linkage between upper- and lower-level PV anomalies; see the PV distributions on the 290 and 310 K isentropic surfaces for 2 March 1982 in Lanzinger et al. (1991). Immediately downstream of the Alps there is, in the model simulations, a dipole of PV anomalies leading to a strong retardation of the flow there with velocities near stagnation being realized. No detailed mesoscale observational data exist to corroborate this prediction as yet.

The nature of mountain flows depends strongly on the Froude number. For flows with low Froude number (say less than 1) there is an increasing tendency for flow to be around rather than over the mountain. For Froude numbers in excess of 1 then there is a larger component of the flow that is over the mountain. The extent to which there is a sharp transition between these flow regimes is a matter of current research; it is likely to depend strongly on the shape of the mountain and on the Rossby number. There has also been recent interest in the generation of the wake behind mountains with low Froude number flow. A pair of counterrotating vortices occurs downstream in such a mountain flow; a straightforward inviscid mechanism capable of producing these structures exists. This is by the baroclinic generation of horizontal vorticity that is then tipped into the vertical as the air ascends over the mountain; see Smolarkiewicz and Rotunno 1989. As those authors point out, this mechanism does not create PV anomalies. It is apparent, however, that if the Froude number is low enough a flow, with no surface friction, may exhibit hydraulic jumps that via small-scale dissipation imply a production of PV anomalies in the flow; see Smith (1989) and Schär and Smith (1993a,b). These anomalies have the sense of rotation of the inviscid vortices just mentioned, namely, for a westerly flow in the Northern Hemisphere a negative PV anomaly north and a positive anomaly to the south of the mountain.

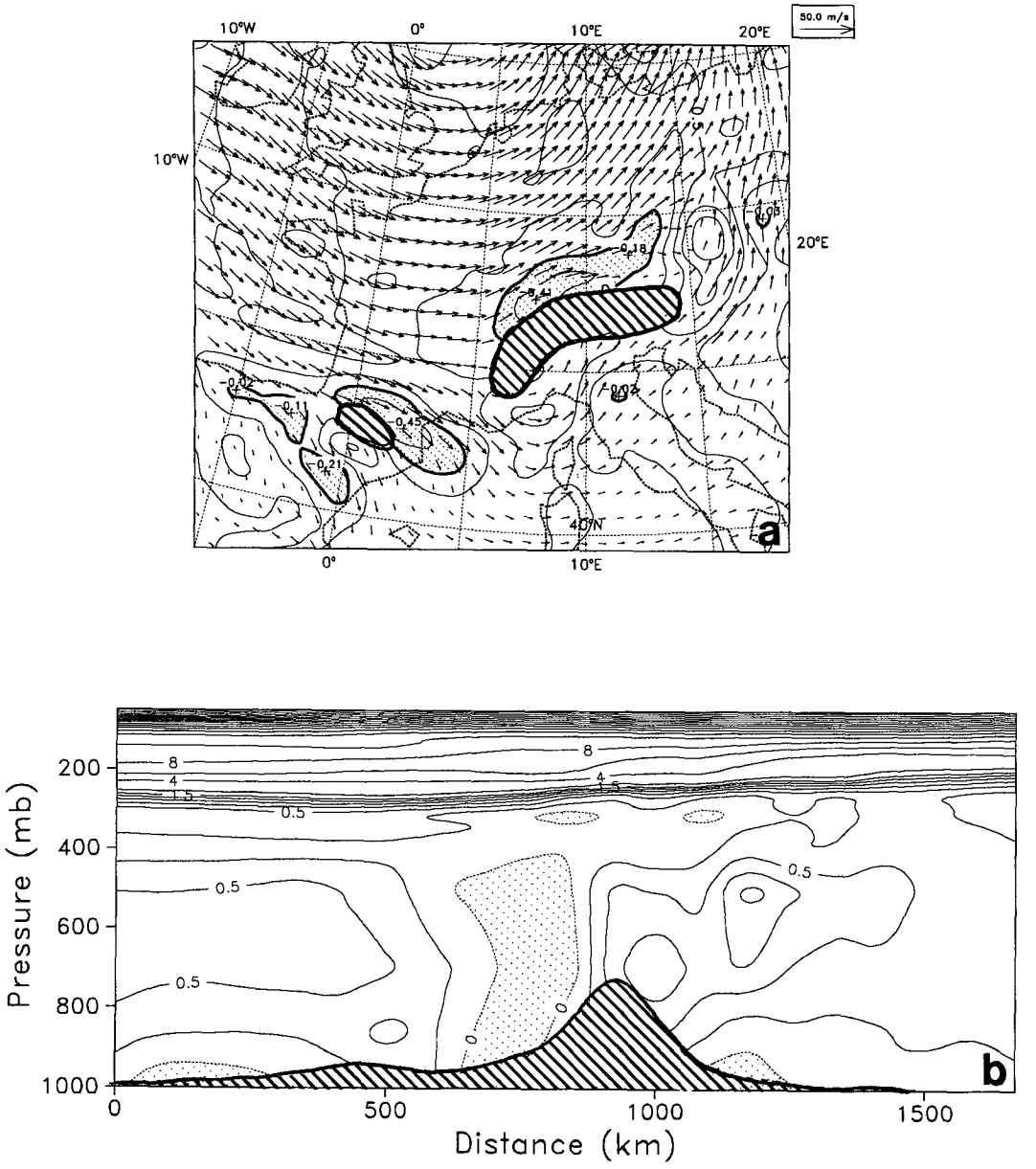

FIG. 19. A 24-h forecast from a rerun of the ECMWF T-213 model for 1200 UTC 8 October 1987 (IOP-A). (a) Contours of PV with negative regions dotted and wind vectors at 850 mb. (b) A N–S cross section viewed from the west along 10.25°E of the PV with negative values dotted. The horizontal resolution is 0.75°, and the model orography is hatched.

In the case of Alpine flow discussed in this paper the Froude number is of order unity. The flow is characterized by being composed of regions where it is around and regions where it is over the mountain. The numerical model results, even in the inviscid case, indicate that the Froude number, of unity, is not low enough to generate wave breaking or hydraulic jumps. The PV anomalies found in the inviscid nonlinear calculation are, therefore, likely to be attributable to numerical errors. It is noteworthy that these errors, because they are in the form of dissipation truncation errors, are likely to have exactly the same structure as those produced by the local zones of dissipation had there been a wake. It is our belief that the observed anomalies of PV presented in section 2 and those found in the idealized simulations with a frictional boundary layer in section 4 are much larger than those found in the low Froude number "inviscid" studies. Hence, the neglect of boundary-layer processes commonly made in theoretical work on mountain wave dynamics may be an extreme limitation on their applicability to the problem of explaining the potential vorticity of the natural phe-

nomenon. It is tantalizing, however, that the PV signature with frictional processes at moderate Froude number and for essentially inviscid flow at low Froude number is rather similar. This is likely to be due to the controlling influence of turbulent mixing in both cases. Even the strong flow retardation noted immediately downstream of the Alps in the simulations here is similar to that due to the counterrotating lee vortices at low Froude number. The aim of this paper has been to highlight the PV structure of observed mountain flows and to concentrate on the mechanism of PV anomaly generation by boundary-layer processes at mountains. It is clear that the pragmatic approach taken here to interpret the observed anomalies of PV needs to be accompanied by a more systematic study of the sensitivity of the results to Froude and Rossby number as well as to the boundary-layer formulation.

It is apparent that, at least for parallel flow, the Alps act as a substantial source of large amplitude PV anomalies throughout the lower troposphere. These are associated with ageostrophic flow near the Alps, but ultimately, away from the mountain geostrophic adjustment will occur while the PV anomalies will persist. The role of the negative potential vorticity on the flow remote from the mountain has not been considered here but is an important question. A diagnostic study is now underway to examine whether in high-resolution forecast models, such as that used by ECMWF, there is significant production of PV anomalies near major mountain ranges. Preliminary results indicate that at least the Alps and the Pyrenees frequently act in this way. As an example we show, in Fig. 19, an ECMWF T-213 "forecast" for the German Front Experiment IOP-A. This is a 24-h forecast from a rerun of this case using the high-resolution model that became operational in September 1991. In plan view and in vertical cross section the large PV anomalies are obvious—both around the Alps and the Pyrenees. The dependence of these anomalies on the flow parameters, such as the Froude number, and on boundary-layer processes is a subject for further research. Here, the probable ubiquity of mountain-generated PV anomalies is noted as is the fact that they may have important implications for mesoscale and synoptic-scale dynamics of the atmosphere.

Acknowledgments. This research was initiated during a visit by Hans Volkert to the JCMM at Reading and was further expedited during a 3-month visit by Alan Thorpe to DLR; financial support for these visits from DLR and the Meteorological Office is gratefully acknowledged. We are indebted to Mike Pedder and Sid Clough for supplying, respectively, the mesoscale objective analysis programmes and software to display analyzed data fields, which we used in this study. We thank Mariano Hortal for carrying out the rerun with the T-213 model of ECMWF and Paul Berrisford for making available the PV diagnostics program for ECMWF data. Comments from Ron Smith and Christoph Schär improved the discussion of the context of our results to current mountain flow research. G. Jacob and U. Mayer competently finalized the figures.

REFERENCES

Cooper, I. M., A. J. Thorpe, and C. H. Bishop, 1992: The role of diffusive effects on potential vorticity at fronts. *Quart. J. Roy. Meteor. Soc.*, **118,** 629–647.

Dempsey, D. P., 1989: Insights into Alpine lee cyclogenesis from numerical simulations of moderately rotating, low Froude number flow past three-dimensional obstacles. Preprints, *Int. Conf. Mountain Meteorology and ALPEX,* Garmisch-Partenkirchen, Deutsche Meteorologische Gesellschaft, 87–89.

Egger, J., and K. P. Hoinka, 1992: Fronts and orography. *Meteor. Atmos. Phys.*, **48,** 3–36.

Eliassen, A., 1968: On mesoscale mountain waves on the rotating earth. *Geophys. Publ.*, **27,** 1–15.

Heimann, D., 1990: Three-dimensional modeling of synthetic cold fronts approaching the Alps. *Meteor. Atmos. Phys.*, **42,** 197–219.

Hoinka, K. P., and H. Volkert, 1987: The German Front Experiment 1987. *Bull. Amer. Meteor. Soc.*, **68,** 1424–1427.

——, and ——, 1992: Fronts and the Alps: Findings from the Front Experiment 1987. *Meteor. Atmos. Phys.*, **48,** 51–75.

Kurz, M., 1990: The influence of the Alps on structure and behaviour of cold fronts over southern Germany. *Meteor. Atmos. Phys.*, **43,** 61–68.

Lanzinger, A., and R. Steinacker, 1990: A fine mesh analysis scheme designed for mountainous terrain. *Meteor. Atmos. Phys.*, **43,** 213–219.

——, H. Pichler, and R. Steinacker, 1991: ALPEX-Atlas: Case studies of ALPEX–SOP cyclones in the western Mesiterranean. 2d ed. Österreichische Beiträge zu Meteorologie und Geophysik, Heft 4, ZAMG-Publ. Nr. 338. [Available from Zentralanstalt fuer Meteorologie und Geodynamik, Hohe Warte 38, A-1191 Wien, Austria.]

Mattocks, C., and R. Bleck, 1986: Jet streak dynamics and geostrophic adjustment processes during the initial stages of less cyclogenesis. *Mon. Wea. Rev.*, **114,** 2033–2056.

Schär, C., 1993: On the diagnosis of the potential vorticity flux: A generalization of Bernoulli's theorem. *J. Atmos. Sci.*, **50,** inpress.

——, and R. B. Smith, 1993a: Shallow-water flow past isolated topography. Part I: Vorticity production and wake formation. *J. Atmos. Sci.*, **50,** 1373–1400.

——, and ——, 1993b: Shallow-water flow past isolated topography. Part II: Transition to vortex shedding. *J. Atmos. Sci.*, **50,** 1401–1412.

Smith, R. B., 1980: Linear theory of stratified hydrostatic flow past an isolated mountain. *Tellus,* **32,** 348–364.

——, 1982: Synoptic observations and theory of orographically disturbed wind and pressure. *J. Atmos. Sci.*, **39,** 60–70.

——, 1989: Comment on "Low Froude number flow past three-dimensional obstacles. Part I: Baroclinically generated lee vortices." *J. Atmos. Sci.*, **46,** 3611–3613.

Smolarkiewicz, P. K., and R. Rotunno, 1989: Low Froude number flow past three-dimensional obstacles. Part I: Baroclinically generated lee vortices. *J. Atmos. Sci.*, **46,** 1154–1164.

Thiebaux, H. J., and M. A. Pedder, 1987: *Spatial Objective Analysis.* Academic Press, 299 pp.

Thorpe, A. J., and S. A. Clough, 1991: Mesoscale dynamics of cold fronts: Structures described by dropsoundings in FRONTS 87. *Quart. J. Roy. Meteor. Soc.*, **117,** 903–941.

Thorsteinsson, S., 1988: Finite amplitude stratified air flow past isolated mountains on an f-plane. *Tellus,* **40A,** 220–236.

Volkert, H., and C. H. Bishop, 1990: The semi-geostrophic Eady problem as a testbed for numerical simulation of frontogenesis. *Tellus,* **42A,** 202–207.

——, M. Kurz, D. Majewski, T. Prenosil, and A. Tafferener, 1992: The front of 8 October 1987: Predictions of three mesoscale models. *Meteor. Atmos. Phys.*, **48,** 179–191.

Wahba, G., and J. Wendelberger, 1980: Some new mathematical methods for variational objective analysis using splines and cross validation. *Mon. Wea. Rev.*, **108,** 1122–1143.